An enclosed live-imaging platform to reveal ultrasound-inflicted mechanolysis and wound healing response

Ziyue Bai[1], Zaimeng Li[2], and Yue Shao[1,*]

[1] Institute of Biomechanics and Medical Engineering, Department of Engineering Mechanics, School of Aerospace Engineering, Tsinghua University, Beijing 100084, China; [2] Institute of Fluid Mechanics, Department of Engineering Mechanics, School of Aerospace Engineering, Tsinghua University, Beijing 100084, China

* Correspondence should be addressed to Y. Shao (yshao@tsinghua.edu.cn)

ABSTRACT

Focused ultrasound (FUS) technology as a non-invasive therapy has been widely adopted in medical and life science research. Although various physical and biological effects of FUS have been well-documented, there is still a lack of understanding and direct evidence on the biological mechanism of therapeutic cell ablation caused by high-intensity ultrasound (HIFU) and the subsequent wound healing responses. Herein, this study designed and built an enclosed cell culture device that can synergistically combine non-invasive FUS stimulation and long-term live-cell imaging, serving as an in vitro platform to explore both short and long-term biological effects of ultrasound. Further, the process, mechanism and wound healing response of cell ablation induced by HIFU were studied, revealing a unique mechanism, termed ultrasound-inflicted mechanolysis, that is mediated by growing cavitation air bubbles under confined contact with cells. This discovery provides a previously unappreciated mechanism for understanding the biomechanical principles of ultrasound-based ablative therapy. We also found a post-ablation phantom layer (PAPL) remaining attached to neighboring live cell monolayer after HIFU stimulation. Such PAPL serves as a guiding cue for collective cell migration during post-ablation wound healing process, thereby providing a biomimetic model for studying wound healing after HIFU-inflicted damage. Together, the findings of this study might provide theoretical and technological basis for advancing our understanding of the biological effects of ultrasound-based ablative therapy and inspiring clinically relevant applications in the future.

INTRODUCTION

In recent years, focused ultrasound (FUS) technology has attracted extensive attention as a non-invasive therapeutic modality and has rapidly advanced in various research areas[1-3]. Currently, the most common application of therapeutic FUS is in the ablation of tumors[4, 5]. Furthermore, FUS exhibits deep penetration and high spatial precision in comparison to other therapeutic physical stimuli. Low-frequency focused ultrasound (frequency < 1MHz) can non-invasively focus within the cranial region[6] and it can be combined with other therapeutic modalities such as microbubbles and phase-change liquid droplets[7]. By promoting transcellular endocytosis, inducing endothelial cell membrane opening, forming cavities or channels within the cytoplasm, and opening tight junctions between endothelial cells, FUS facilitates the delivery of therapeutic agents, *e.g.*, cisplatin[8], doxorubicin[9, 10], mistletoe lectin-1 (ML1)[11], trastuzumab[12], and genetic materials[13] across the blood-brain barrier (BBB)[14, 15] or blood-tumor barrier (BTB)[16-18]. On neuroregulation, FUS can either inhibit or activate neural activity[19-21], showing significant potential in analgesia[22]. Its stimulation of the hepatic portal venous plexus holds promise as a non-pharmacological treatment for glucose homeostasis dysregulation[23]. Moreover, FUS has been applied in thrombolysis[24], as well as in therapeutic research related to inflammation[25, 26]. Overall, FUS-based therapeutic techniques offer vast avenues for clinically relevant applications.

The therapeutic principle of FUS technology is based on the energy accumulation generated when ultrasound waves are focused on specific areas in tissues, leading to thermal or mechanical effects. Subsequently, a series of biological effects are induced to achieve therapeutic objectives. The thermal effect of focused ultrasound refers to the higher energy accumulation at the focal point, causing a significant temperature increase in the targeted tissue compared to non-focal tissue. Different temperature elevation can achieve varying regulatory effects[27, 28]. For instance, using low-intensity focused ultrasound (LIFU) can mildly increase the temperature (*e.g.*, a rise of 2-6℃) of the targeted

63 tissue as a form of local hyperthermia[29]. On the other hand, employing high-intensity focused ultrasound
64 (HIFU) for a short duration can heat the targeted tissue to a high temperature (above 55°C), leading to
65 coagulative necrosis and "thermal ablation" of tissue. The mechanical effects of FUS primarily include
66 cavitation effects, which are divided into stable cavitation and inertial cavitation. Stable cavitation refers
67 to the stable oscillation of microbubbles in the focal region under the effect of pressure waves. Inertial
68 cavitation involves the drastic volume changes of microbubbles under the influence of strong pressure
69 waves, ultimately leading to their rupture and generating shock waves[30]. Despite considerable research
70 on the physical effects of FUS, the investigation into the biological effects mechanism such as cell
71 ablation induced by HIFU, and the subsequent wound healing response, remains limited. This hinders a
72 comprehensive understanding of the mechanisms underlying HIFU therapy and limits improvements
73 and optimizations in ultrasound therapeutic methods. Therefore, it is critically needed to explore the
74 mechanism of HIFU-induced cell ablation and associated wound healing responses.

75 To investigate the mechanisms of ultrasound therapy, *e.g.*, HIFU-induced cell ablation, it is
76 essential to develop experimental models that can simulate multicellular damage and repair processes
77 under ultrasound treatment in vitro. Traditionally, for in vitro studies on the biological effects of
78 ultrasound, researchers would typically expose cells to FUS treatment and then observe them under a
79 microscope[31-33]. This method is relatively simple and convenient but lacks real-time observation of cell
80 responses during FUS stimulation, which is necessary for studying short-term cell responses. Currently,
81 real-time monitoring devices for studying ultrasound-induced responses mainly rely on either an upright
82 or an inverted microscope. For example, Zhihai *et al*.[34] integrated a FUS device with an upright
83 microscope, placing the focused ultrasound transducer beneath the culture dish at a 45-degree angle.
84 When cells were stimulated with FUS, the incident sound waves were focused to the bottom of the
85 culture chamber through a waveguide material, then reflected at a right angle to reach an absorber.

86 Simultaneously, real-time imaging was performed by immersing the objective into the upright-placed
87 cell culture dish during stimulation. Recently, Yao-Shen *et al*.[35] combined a FUS device with an
88 inverted microscope, with the FUS transducer was immersed vertically into the cell culture medium.
89 However, these setups required immersing the objective lens or ultrasound transducer into an open cell
90 culture environment, leading to a significant risk of contamination. Despite that they might be suitable
91 for short-term experiments (0-30 minutes), they are insufficient to support continuous studies on the cell
92 ablation mechanisms and subsequent wound healing responses induced by HIFU. This hinders the
93 exploration and understanding of relevant mechanisms. Therefore, it is imperative to develop new
94 technologies that integrate non-invasive ultrasound stimulation, real-time live-cell imaging, and long-
95 term cell culture into a single platform. This is a key technical challenge that this study aims to address.
96 Herein, this study has designed and constructed a fully enclosed cell culture device (ECCD)
97 capable of simultaneously achieving non-invasive ultrasound stimulation and long-duration live-cell
98 imaging. This device serves as an experimental platform for exploring the biological effects of FUS.
99 Unlike previously reported open culture systems, this platform allows for real-time and programmable
100 FUS stimulation of cells in the target region, while also enabling long-term, online monitoring of
101 cellular responses using an inverted microscope. We applied this platform to obtain a stereotypic focal-
102 area geometry under FUS, and analyze the biophysical effects involved in different sub-regions of the
103 focal-area, including short and long-term cellular responses during and after HIFU-induced cell ablation.
104 This study not only provides direct experimental evidence and insights into classical thermal and
105 mechanical effects of FUS, but also reveals previously unappreciated biomechanical mechanisms
106 underlying the cell damage and wound healing involved in FUS-based ablative therapy.
107
108 **RESULTS**

109 **Design of an enclosed cell culture device compatible with FUS stimulation and long-term live-**
110 **cell imaging**

111 In order to simultaneously achieve non-invasive FUS stimulation and long-term live-cell
112 imaging, this study established an enclosed cell culture device (ECCD). Through optimized design of
113 the acoustic path, acoustic windows, and sound-absorbing materials, the device enables FUS to act on a
114 focal cell culture area at the bottom of the cell culture device (**Fig. 1a**). Meanwhile, real-time imaging
115 captures changes and responses of the cultured cells in this region. Specifically, this design allows the
116 FUS to be emitted from the transducer, reach the outside of the cell culture device via the coupling
117 device, pass through the acoustic window, and further propagate in the cell culture medium. Ultrasonic
118 waves then focus at the bottom of the ECCD, where a glass coverslip for cell culture is horizontally
119 positioned. The axis of the ultrasound cone forms a 45-degree angle with coverslip, and are
120 subsequently reflected at a 45-degree angle. Such reflected waves pass through the exit acoustic window
121 and are absorbed by a sound-absorbing material attached to the window, thereby avoiding additional
122 reflections that may affect the focused acoustic field within the cell culture device.

123 The ECCD is assembled from multiple components. To meet requirements for FUS stimulation
124 and routine cell culture, we adopted a four-sided pyramid structure (**Fig. 1b**). The left and right sides of
125 the device are inclined at 45-degree against the bottom surface, with circular and rectangular windows
126 are opened on each, henceforth referred to as "entrance acoustic window (EnAW)" and "exit acoustic
127 window (ExAW)", respectively. Both acoustic windows are sealed with 1 mm thick sheet of acoustically
128 transparent material. This allows the FUS beam to transmit with extremely low loss along the expected
129 acoustic path while avoiding direct contact between the ultrasound transducer and the liquid inside the
130 culture device. A circle of grooves is extended from the inner edge of the EnAW and ExAW for
131 positioning and stabilizing the acoustically transparent sheet. To ensure correct positioning and light
132 contact of the ultrasound transducer coupler and the EnAW, a set of protruding keys were manufactured

133 at the inner rim of the EnAW to restrict the translational movement of the coupler. A circular opening
134 and recess structure are made at the bottom of the ECCD to allow the attachment of a coverslip for cell
135 culture (**Fig. 1b**).

136 Considering the relatively large size of the FUS transducer, a coupler is required to integrate it
137 with the ECCD. To match the shape of the ultrasound transducer and the ultrasound cone, the coupler is
138 designed to contain a conical head (**Fig. 1c&d**), which has a circular opening covered with a 1 mm thick
139 acoustically transparent sheet. The coupler also features a set of protruding keys complementary to those
140 on the rim of the EnAW of ECCD, ensuring the centered assembly and tight fit between them (**Fig. 1e**).
141 During operation, the coupler is filled with degassed water and connected through inlet/outlet ports to a
142 circulation system for cooling. The rear part of the coupler is a cylindrical cavity for placing the
143 transducer, before the coupler is sealed by a lid and a silicone ring upon mechanical tightening.

144 To examine whether the focused sound field in the device meets the design expectations, we
145 conducted multiphysics simulations using COMSOL. For simplicity, a two-dimensional model was used
146 (see **Methods** for details). The calculated sound pressure field, sound pressure level field
147 (**Supplementary Fig. 1c**), and sound intensity field (**Fig. 1f**) were normalized and plotted as heat maps.
148 These results showed that the ultrasound waves converged along the expected two-dimensional cone to
149 reach the focal point. Subsequently, they reached the ExAW along the ideal reflection angle and were
150 absorbed by the sound-absorbing material (modeled as a perfect matching layer in the simulation).
151 These results clearly indicate a focal ultrasound stimulation at the target region of the cell culture area,
152 with significantly lower level of ultrasound outside of the focal region. Similar results can be observed
153 in the sound intensity field image as well. Such focused stimulation performance meets the goal of our
154 device design. To evaluate the importance of sound-absorbing materials, we attempted to remove it in
155 the simulation (**Supplementary Fig. 1d**) and then observed highly disordered, non-focal sound pressure

156 field and sound pressure level field in the device (**Supplementary Fig. 1e**), as illustrated by sound
157 waves undergoing multiple reflections. Under such condition, the energy cannot be accumulated at the
158 focal point, and a stable energy distribution cannot be calculated in the steady-state sound intensity field.
159 Therefore, the sound-absorbing material in the design of ECCD is crucial for ensuring a stable and
160 predictable focused sound field. In addition, we compared the acoustic field of ECCD with that
161 generated in a conventional upright imaging system, which was previously used to stimulate cells with
162 ultrasound (**Supplementary Fig. 2**). Our simulation results showed that in contrast to the focal field
163 formed in the ECCD, the conventional system only generated disordered acoustic field despite the use of
164 a focused ultrasound transducer, due to the lack of design to optimize the acoustic path. Therefore, our
165 results implicate the importance of ECCD device design to assure desirable combination of focal
166 stimulation and unobstructed live-imaging.
167

168 **An experimental platform for FUS stimulation and live-cell imaging based on ECCD**

169 In order to integrate ECCD with laser confocal microscopy, a carrier system was designed. This
170 system allows the transducer, coupler, and culture device to move freely in three dimensions within the
171 microscope's field of view, facilitating optical focusing and field-of-view selection. To this end, a three-
172 axis displacement platform, referred to as the primary displacement system, was employed (**Fig. 2a&b**).
173 This system also mechanically isolates the weight of the ultrasound transducer, coupler, and culture
174 device, from the microscope platform, thereby ensuring minimal disturbance to the optical systems as
175 well as universal applicability to different kinds of optical setups. Furthermore, ensuring alignment and
176 close contact between the ultrasound transducer coupler and the culture device is crucial for maintaining
177 the stability and predictability of the acoustic pathway during experiments. Therefore, a secondary
178 displacement system was mounted on the primary platform to control the relative motion between the
179 coupler and the culture device. This system, with only one degree of freedom in the vertical direction

180 (Z-axis), independently controls the vertical motion and applies additional load to achieve precise
181 alignment between the coupler and the EnAW. With such a two-level carrier system, independent
182 adjustments can be made to the acoustic pathway as well as the optical path relative to the microscope,
183 decoupling the control of ultrasound stimulation and that of microscopic imaging.

184 High-precision 3D printing was chosen to manufacture the coupler and ECCD. The ECCD was
185 made from MED610 photopolymer resin, which is commonly used in orthopedic and oral surgery[36] and
186 expected to exhibit good biocompatibility, thermal stability, and chemical stability under cell culture and
187 ultrasound stimulation conditions. It also demonstrates mechanical stability to prevent deformation,
188 breakage, fatigue, and creep during assembly and experiments. The coupler was made from ABS
189 photopolymer resin (acrylonitrile-butadiene-styrene copolymer) using high-precision 3D printing (**Fig.**
190 **2c&d**), due to the robustness, density, and stability of the materials.

191 For the acoustic windows mounted on the ECCD and the coupler, 1mm-thick acoustically
192 transparent material was used to both ensure seamless coupling and avoid window bending due to liquid
193 pressure under working conditions. These acoustic windows should be made from materials that do not
194 significantly reflect sound waves at its interface with the culture medium (considered as water). Firstly,
195 several common laboratory materials were tested for acoustic impedance, from which
196 polydimethylsiloxane (PDMS) was found to have an impedance value close to that of water (**Fig. 2e&f**).
197 Subsequently, different PDMS were tested, and the acoustic impedance of PDMS slab at 4:1 mixing
198 ratio was found closest to that of water at the same temperature. Therefore, PDMS with base: curing
199 agent ratios at 4:1 was used for making acoustic windows. Before conducting experiments, the primary
200 displacement platform carrying the ultrasound stimulation system and the secondary displacement
201 platform carrying the ECCD (**Fig. 2g**) are assembled and mounted on the optical table of the microscope
202 (**Fig. 2h**).

203 In addition, we calibrated the acoustic field generated by the FUS transducer used in this study.
204 In particular, the calibration was conducted using a hydrophone to measure the sound intensity field near
205 the focal plane of the transducer. The results showed that when the input voltage to the transducer was
206 20 V, the frequency 1 MHz, the repetition frequency 10 kHz, and the duty cycle 30% for burst waves,
207 the -3 dB focal region (where the sound intensity dropped to 50% of the maximum intensity) on the X-Y
208 plane (perpendicular to the axis of the focusing acoustic cone) was approximately a circular area with a
209 diameter of 3 mm; while on the X-Z plane, the -3 dB focal region was an elliptical shape with a major
210 axis of about 18 mm and a minor axis of about 3 mm (**Supplementary Fig. 3a**).
211 Given that thermal effect due to HIFU is inevitable during experiments, we studied the dynamics
212 of average temperature change at the focal region. Specifically, we used a high-speed thermistor
213 measurement method. Specifically, a T25 culture bottle with a thermistor attached to the bottom and
214 filled with water was placed on the path of the FUS (**Supplementary Fig. 3b**). To ensure high thermal
215 sensitivity and minimal scattering of the acoustic waves, the thermistor was made from a platinum wire
216 (50 μm in diameter). To measure the average temperature over the focal region, the platinum wire was
217 bent and attached to a 3×3 mm^2 square area matching the size of the focal region (**Supplementary Fig.
218 3c-e**). Our results showed that under FUS stimulation, the temperature at the focal region could rise and
219 reach a steady state within about 5 s, and drop to the environmental temperature within 3 s after the FUS
220 was stopped, thus demonstrating the rapid temperature response at the focal region. Moreover, the target
221 temperature of the focal region can also be modulated by varying the ultrasound intensity and the duty
222 cycle of burst waves (**Supplementary Fig. 3f&g**).
223

224 **HIFU-induced cell ablation does not show significant correlation with ultrasound-caused
225 thermal effect**

226 To mimic the interaction between FUS and tissues (especially epithelial tissues, which are
227 commonly involved in ultrasound therapy), this study selected epithelial monolayer of Madin-Daby
228 canine kidney cells (MDCK cells) as an in vitro model. Firstly, to validate the compatibility of ECCD
229 with cell culture, MDCK cells were plated in ECCD and regular 60 mm culture dish and cultured for 2
230 days. At 50% and 100% confluence, no significant difference was observed between above two groups
231 in cell proliferation and epithelial colony morphology (**Fig. 3a**). In order to observe the shape and size of
232 focal region produced by FUS on MDCK monolayer in ECCD, we next set to simultaneously investigate
233 the temperature change of focal region and cell ablation under FUS stimulation. Although
234 abovementioned results from thermistor experiment showed the dynamics of average temperature
235 change in the focal region, it was not suitable for measuring the temperature field distribution of the
236 focal area. To characterize the temperature field, custom-made thermochromic tapes were used. These
237 tapes contained thermochromic inks with pre-calibrated color-changing temperatures of 31, 38, 45, and
238 65°C in red, yellow, green, and purple, respectively, and were mixed at volume ratio of 4:2:2:1. These
239 yinks changed color from brick red at room temperature to green, blue, purple, and milky white at
240 temperatures of 34, 38, 43, and 62°C, respectively (**Fig. 3b**). These tapes were applied to the bottom of
241 the culture device before FUS experiments, and the color changes were recorded to reconstruct the
242 temperature field changes during ultrasound stimulation. Additionally, to detect cell ablation after
243 ultrasound stimulation, Live dye was used to label the entire monolayer of MDCK cells at 100%
244 confluence before the experiment. Of note, while Live dye emits a strong green fluorescence (FITC)
245 inside cells with intact plasma membrane, it produces little or no fluorescence signal outside the cell or
246 once cell membrane was ruptured, thereby serving as an indicator of cell ablation. It is also important to
247 note that the disappearance of FITC signal only reflect cell ablation, not necessarily cell detachment.

248 Given that HIFU-based thermal effects are widely believed to be associated with ultrasound-
249 induced cell ablation in previous studies[4, 27], we next compared the changes in the focal region
250 temperature with the distribution of cell ablation. The "temperature field" was henceforth defined based
251 on the images of the thermochromic tape, with particular attention to the region where color change (*i.e.*,
252 temperature change) occurred. This temperature field could clearly visualize the focal area under FUS
253 treatment. Correspondingly, the images of cells captured under FITC fluorescence were henceforth
254 defined as the "cell field". Specifically, we define areas where cells were ablated (shown by the
255 disappearance of fluorescence during FUS treatment) as the "cell ablation area", and an elliptical-like
256 enveloping area that encloses all cell ablation area was defined as the focal area of cell field. Our results
257 indicated that under FUS stimulation, the focal area of the temperature field reached a steady state
258 within a short time (1-10 s). After stopping ultrasound, the focal area of the temperature field also
259 returned to ambient temperature within a relatively short time (**Supplementary Fig. 4a**). This was
260 consistent with the temperature change dynamics measured by thermistor-based method
261 (**Supplementary Fig. 3f&g**).
262 Of note, our results showed that the contours of the temperature field and the cell field were
263 roughly elliptical, with the major axis direction along the direction of ultrasound propagation (**Fig.**
264 **3c&d**). By measuring the lengths of the major and minor axes of the elliptical outline of the focal region
265 of the temperature field and cell field (**Fig. 3e**), we observed a positive correlation between FUS
266 intensity and the size of focal region of the temperature field, as well as that of the cell field. As
267 expected, similar correlation was also observed between FUS treatment time and above focal regions
268 (**Fig. 3c&d**).
269 However, by comparing the cell ablation area with the focal area of the temperature field, it is
270 clear that the focal area of the temperature field showed continuously decreasing temperature from the

271 center to the periphery, while the distribution of the cell ablation area was not necessarily continuous or
272 following the temperature gradient. Notably, the cell ablation area was a hollow elliptical shape under
273 conditions of high ultrasound intensity (transducer voltage 50 V, exposure time 3 min), and it became a
274 circular elliptical band under conditions of lower ultrasound energy (transducer voltage 20 V, exposure
275 time 3min), with non-uniform cell ablation within it (transducer voltage 40 V). Further quantitative
276 comparative analysis revealed no significant correlation in terms of shape and size between the cell
277 ablation area and the focal region of the temperature field (**Fig. 3f&g**). These observations suggested that
278 although changes in the temperature field occurred as expected within the elliptical focal region, the
279 continuous changes in the temperature field and the non-continuous, non-uniform changes in the cell
280 ablation area were inconsistent with the conventional understanding of ultrasound-based thermal
281 ablation theory. This implies that mechanisms other than thermal effects might exist for cell ablation
282 under FUS.

283 To further demonstrate that the thermal effects within the FUS focal area were insufficient to
284 ablate cells within this region in the short experimental observation time of this study, we placed the
285 ECCD (with a monolayer of MDCK cells at over 90% confluence) into water baths at 65°C and 85°C,
286 respectively, for 5 minutes. Compared with the untreated group, the proportion of cell ablation caused
287 by short-term treatment was less than 10% in both 65°C and 85°C groups (**Supplementary Fig. 4b&c**).
288 This is significantly different from the proportion of the cell ablation area within the focal region of cell
289 field under FUS stimulation. These results indicated that cell ablation produced under FUS stimulation
290 in a short time and the associated thermal effects in the focal area were not significantly correlated in a
291 global manner. Therefore, it is necessary to explore cell ablation mechanisms beyond thermal effects.
292

293 **HIFU-induced cell ablation is associated with cavitation bubbles**

294 To explore cell ablation mechanisms under FUS stimulation beyond global thermal effects, we
295 performed experiments using MDCK cells expressing red fluorescent protein in cell nuclei (H2B-RFP).
296 Firstly, we applied Live dye to visualize cell ablation region. **Fig. 4a** shows a typical structure of the
297 cell-ablation area after HIFU treatment, which features an elliptical ablation band surrounding a central
298 area with streak-like ablation domains and a small, central, high-temperature domains. Specifically,
299 when the FUS was activated for a few seconds, the streak-like ablation pattern appears near the
300 nucleation-like high-temperature domain (**Fig. 4a**), and expands from the side proximal to the incident
301 FUS waves, as shown in **Supplementary Fig. 5**. Of note, there were no bubbles in the streak-like
302 ablation domains during FUS treatment, suggesting it is perhaps starts from a combination of high-
303 temperature and shear force and then continued to expand due to acoustic streaming driven by the
304 nonlinear effect of ultrasound[37].In the meantime, when the FUS was activated for a few seconds, a large
305 number of bubbles gradually appeared near the side proximal to the incident FUS waves, causing cell
306 ablation at this site, which evolved into a crescent-like shape and eventually a complete elliptical
307 ablation band. Even after the cessation of FUS, some bubbles remained in the crescent-like region (**Fig.**
308 **4b**). These bubbles are opaque under the bright field, but almost transparent in the fluorescent channel,
309 with only a halo around the edge. These data suggest that above-observed cell ablation is closely
310 associated with bubble formation under FUS.
311 To further investigate the relationship between FUS-induced bubbles and cell ablation, we used
312 Dead dye to monitor cells that died during FUS treatment in real time. A band of bubbles (black arc
313 shown in **Fig. 4c&d**) first appeared, wherein bubbles were constantly generated, expanded and finally
314 burst under FUS. Due such mechanical effect of this band of bubbles, cells in the corresponding region
315 were ablated rapidly, as reflected by the presence of the Dead dye signal. Such ablated cell monolayer
316 eventually broke down and fractured and left a narrower void band. Meanwhile, we did not observe

317 notable temperature rise in this region, ruling out that the bubbles in this region are caused by the
318 heating and boiling of the liquid in this region. Therefore, we reason that this phenomenon might be
319 attributed to the inertial cavitation phenomenon.

320 Strikingly, we observed a large number of steadily expanding bubbles in the crescent-like region
321 proximal to the incident FUS waves. These bubbles, in contrast to above-mentioned inertial cavitation,
322 remain stable and expanding without bursting, in the absence of insignificant temperature increase. This
323 suggested that these bubbles and corresponding cell ablation in this particular region might reflect a
324 mechanism different from canonical effects such as thermal-ablation or cavitation bubble collapse.

325 To further illustrate the relationship between stable FUS-induced bubbles and cell ablation
326 observed in the proximal region of the crescent-like region, we treated the cells with a pulsed FUS of
327 varying intensity with a duty cycle of 10% and a pulse repetition rate of 1 kHz (**Supplementary Fig. 6**).
328 Compared with abovementioned continuous FUS waves, pulsed FUS with the same transducer input
329 voltage showed greatly reduced temperature within the focal region. Under pulsed FUS, the streak-like
330 ablation domains in the central region of the focal plane are still evident, further indicating it is likely
331 due to non-cavitation mechanical effect such as shear stream instead of thermal effect. Importantly, with
332 pulsed FUS, there was no notable formation of stable bubbles, nor formation of elliptical ablation band
333 with stable bubbles or cell ablation associated with it. These results indicate that FUS-induced cell
334 ablation in the unique crescent-like domain requires the formation of stable bubbles.

335 Notably, after cell ablation within the elliptical band, a layer of dead cells remained attached (**Fig.
336 4e**). Bright-field imaging results showed that while this layer of dead cells still appear to connect with
337 the rest of the cell monolayer, its morphology differed significantly from live cells. This suggests that
338 cell ablation under ultrasound may not result in the complete disappearance of cells and their substances
339 but leaves behind a post-ablation phantom layer (PAPL) composed of cellular remnants. Importantly,

340 the connections formed by the cytoskeleton in the phantom layer appear intact, maintaining connections
341 to adjacent live cell monolayer. Although such connections might hold the phantom layer in its original
342 place, it was also observed that after long-term FUS treatment, or at the location where large bubble
343 clusters form, the phantom layer could break away from the substrate (**Fig. 4f**). In this process, even part
344 of the live cell monolayer connected to the phantom layer could be peeled off the substrate. Therefore,
345 abovementioned results indicate a significant correlation between FUS-induced air bubbles and the cell
346 ablation potentially via mechanical interactions between them. This suggests that it is critical to
347 investigate deeper into the mechanical interactions between FUS-induced bubbles and cells.
348 Additionally, the formation of the PAPL in above FUS-induce tissue damage model might represent a
349 previously unappreciated opportunity to recapitulate the wound created by HIFU-based cell ablation.
350

351 **Mechanolysis induced by subcellular bubble formation in the ablation band**

352 Above experiments provided macroscopic level clues regarding a mechanical mechanism
353 underlying HIFU-induced cell ablation mediated by bubbles. To further explore the correlation between
354 bubble formation and cell ablation in the elliptical ablation band at the microscopic level, we observed
355 cellular responses during FUS treatment at single-cell resolution. Live dye was used to track cell
356 viability in real-time. Our results showed that, as ultrasound stimulation proceeded, a subcellular air
357 bubble suddenly appeared where cells are attached. As the bubble grew, the fluorescence intensity of the
358 cell associated with the bubble started to decrease until almost no fluorescence signal could be detected
359 in the whole cell (**Fig. 5a**). Quantitative analysis of the average fluorescence intensity after the
360 appearance of the bubble revealed a rapid decay within a few seconds, followed by a minimally
361 detectable plateau (**Fig. 5b**). These results suggest that as the bubble grows, the cell membrane was
362 broken, leading to the outflow of cellular content and eventually cell death. Statistical analysis indicated
363 that the fluorescence signal of the cell decreased from the level of live cells to the background level in

364 an average time of about 10 seconds after the appearance of the bubble, (**Fig. 5c**). Compared to classical
365 processes like apoptosis or necrosis, this is a remarkably rapid process, implying a different mechanism
366 for cell ablation through mechanical interaction between cells and FUS-induced subcellular bubbles.

367 To investigate the mechanism by which bubbles induce cell ablation, we first needed to
368 determine the relative positions of bubbles and cells. Thus, we performed optical sections and 3D
369 reconstruction of GFP-expressing MDCK cells during FUS treatment. Specifically, there were 10 optical
370 sections (X-Y planes) were acquired along the z-axis, with section spacing 11.29 μm, and the total
371 scanning height 101.62 μm. The lowest optical section was lower than the bottom surface of the cell
372 (where there is no fluorescence), and the top optical section was higher than the top surface of the cell
373 (where there is no fluorescence) to ensure that the 3D reconstruction included the signals across entire
374 thickness of the cell. 3D reconstructed images (**Fig. 5d**) showed that, before bubble formation, the green
375 fluorescence was uniformly distributed within the cell. As the bubble formed, a non-fluorescent circular
376 area appeared inside the cell (from X-Y cross-section). X-Z and Y-Z sections further revealed that the
377 bubble's formation created a low-fluorescence area between the cell's original position and the substrate
378 (coverslip), surrounded by the GFP fluorescence signal of the cell itself, reflecting the bubble might
379 push part of the cell away from the substrate upon its formation. This suggests that under ultrasound
380 treatment, subcellular air bubbles may originate between the cell and the substrate, exerting a repulsive
381 force on the cell.

382 To further confirm that abovementioned bubbles, whose appearance resulted in a low-
383 fluorescence region inside the cell, were indeed formed between the cell and the substrate undeath it, we
384 compared them with another type of bubbles that are known to be positioned above, instead of
385 underneath, the cell, and thus do not generate a repulsive effect. Specifically, our quantitative analysis
386 showed that bubbles that eventually caused cell ablation significantly reduced the fluorescence signal at

387 where they appear, even before the cells died (**Fig. 5e**). Continuing to track these bubbles, we observed
388 that, after ablating the cell at its original location, they continued to attach to the substrate, grow, and
389 reach the culture space above surrounding live cells. In this case, these bubbles were simply positioned
390 above, instead of intruding into, the cells below, and such bubbles did not significantly affect the
391 fluorescence signal from cells underneath (**Fig. 5e; Supplementary Fig. 7a**). The comparison of above
392 two situations suggests that bubbles causing cell ablation and those floating on the cell surface exhibit
393 significant differences in optical effects, with the latter lacking a repulsive effect on the cell. This further
394 supports our hypothesis that bubbles causing cell ablation originate between the cell and the substrate,
395 creating repulsive forces that might eventually rupture the cell.

396 To further substantiate above hypothesis, we investigated the relationship between subcellular
397 bubble formation and cell membrane deformation, we performed Z-stack imaging on MDCK cells that
398 only expressed membrane-GFP during FUS treatment (**Fig. 5f**). To confirm that bubbles only appeared
399 between the cell and the substrate, we scanned only the bottom half of the cell close to the substrate. The
400 scanning height was 16.60 μm, consisting of 5 layers with a spacing of 4.15 μm. Under this setting, the
401 uppermost optical section was at the middle of the cell, and the lowest was below the cell membrane,
402 thus could capture the formation and growth of the bubble along with cell membrane deformation once
403 the bubble formed between the cell and the substrate. Our result showed that a bubble appeared at 7.6 s
404 after FUS treatment, and the membrane-GFP signal enveloping the bubble was also clearly observed
405 (**Fig. 5f**), suggesting that the bubble indeed formed between the cell and the substrate and caused close
406 contact with cell membrane. As the bubble gradually expanded, the membrane-GFP signal enveloping it
407 also expanded, reflecting the direct mechanical repulsive effect of the bubble on the cell membrane.
408 Importantly, at 38 s, the membrane-GFP signal enveloping the bubble no longer exhibited a continuous
409 curved shape but instead showed structures resembling bifurcated cracks, followed by cell rupture. This

410 provided direct experimental evidence that bubble formation and growth caused the expansion and
411 ultimate rupture of the cell membrane (**Fig. 5f**). Additionally, we observed that some bubbles
412 disappeared on their own after formation, and with time, the fluorescence signal of the live cells in their
413 occupied area gradually recovered. This further supports the repulsive effect caused by bubble to the cell
414 (**Fig. 5g**).

415 Altogether, while we do not rule out the possibility that thermal effects by FUS may contribute
416 to the ablation of some cells within the focal zone, the above results suggest that the formation of
417 subcellular bubbles between the cell and the substrate and their repulsive effect on the cell impose
418 significant mechanical loads on the cell membrane, leading to continuous expansion and eventual
419 rupture. This process is distinct from classical mechanisms of ultrasound-induced cell ablation and
420 represents a previously unappreciated mechanism, which we termed ultrasound-inflicted “mechanolysis".

421 Furthermore, whether bubbles exert mechanical effects on the cell nucleus is another important
422 question. Therefore, we conducted FUS stimulation experiments on MDCK cells expressing H2B-RFP,
423 simultaneously using Live dye to monitor cell viability. The results showed that bubbles generally did
424 not form directly beneath the cell nucleus (**Supplementary Fig. 7b**), and the morphology of the cell
425 nuclei in the PAPL did not show significant distortions after cell ablation, suggesting less significant
426 effect of subcellular bubbles on cell nucleus than that on the cell membrane. In some cells, it was indeed
427 observed that when the formation of a bubble occurred near the cell nucleus, it could cause mechanical
428 compression and deformation of the cell nucleus, but not to a degree significant enough to induce
429 notable translocation or rupture of the cell nucleus (**Supplementary Fig. 7c**). This suggests that the
430 mechanical effect of bubbles on the cell membrane may be a critical factor in FUS-inflicted
431 mechanolysis

432 Therefore, based on above findings, the interactions between HIFU-induced bubbles and the cell
433 could be largely grouped into three different types (**Fig. 5h**). When bubbles form between the cell and
434 the substrate, if they may persist for a short time before disappearing, the cell could gradually refill the
435 void space created by the bubble. For bubbles that form and consistently grow between the substate and
436 the cell, they can cause significant deformation of the cell membrane, ultimately leading to
437 mechanolysis of the cell. Finally, as these bubbles further enlarge, they may eventually penetrate
438 through the PAPL and detach from the substrate.

439 To investigate whether this ultrasound-induced bubble generation can be achieved in thicker
440 tissues, we performed FUS treatment (continuous wave) to 3D extracellular matrix made of Matrigel
441 domes attached to the ECCD. As shown in **Supplementary Fig. 8a**, bubbles are continuously generated
442 and expanded in the 3D matrix during the FUS treatment. Z-stack scanning images shown in
443 **Supplementary Fig. 8b** indicated that bubbles are distributed throughout the 3D matrix, indicating that
444 this FUS-induced bubble phenomenon is not limited to monolayer cultured cells in vitro, but also occurs
445 in more physiological-like 3D matrix.

446

447

448 **Collective cell migration and wound healing after HIFU-induced cell ablation**

449 The wound healing response after ultrasound-induced cell ablation holds significant practical
450 implications, yet there is a lack of exploration in previous studies. Using only mechanical scratch or
451 place-holders to create empty space that cells could migrate into does not recapitulate key features of
452 ultrasound-inflicted wounding, such as the residue of cell/tissue debris left at the original place after
453 ultrasound ablation, thereby limiting their applications in understanding subsequent wound healing
454 response. In this study, the HIFU-induced ablation successfully created a unique type of wound, termed
455 the PAPL, within a continuous epithelial monolayer, providing a more biomimetic model of HIFU-

456 inflicted wounding. Herein we apply this model to study the collective cell migration and wound healing
457 after HIFU-induced ablation.

458 To this end, we continued to culture cells in ECCD after HIFU ablation and tracked the
459 migration of the cells close to the wounded PAPL area (**Fig. 6**). Under experimental conditions that
460 allow the PAPL to remain entirely or partially attached to the substrate after ablation, we explored how
461 it might regulate the collective migration of the neighboring live cells and the closure of the wound.
462 Using H2B-mCherry MDCK cell monolayers, we found that live cells actively and directionally
463 extended and migrated towards the area where the PAPL remained after ablation until the ultrasound-
464 inflicted wound was completely closed. During this process, there remained a connection between the
465 PAPL and live cells, and live cells also reconstructed the PAPL during the closure of the wound.
466 Additionally, under conditions where ultrasound was strong enough to cause the detachment of the
467 PAPL, we observed that live cells around the wound area could still migrate into the clear area left at the
468 original place of the PAPL. This indicates that cells are intrinsically able to migrate towards the wound
469 area regardless of the presence of the PAPL. Importantly, during the process of collective cell migration
470 and wound healing, we observed a phenomenon of "fracture" between some "leading cells" at the
471 migration front and the cells behind them, forming new tissue gaps. This implies a process of secondary
472 damage that is generated spontaneously during the repair of the primary wound inflicted by ultrasound
473 ablation) (**Fig. 6b**). This may be due to the different directions and speeds of movement of cells within
474 the cell monolayer nearby the wound. Such secondary damages were often repaired again after the
475 closure of the primary ultrasound-induced wound.

476 To further investigate the influence of the PAPL on the dynamics of collective cell migration and
477 wound healing response after ultrasound ablation, we selected cases where part of the PAPL remained
478 attached to the substrate, and tracked and analyzed the cell migration nearby. As shown in **Fig. 7a**, the

479 live cell monolayer in this case could migrate into both the PAPL and the free area (where the PAPL had
480 detached but still available for live cells to migrate into), providing a basis for analyzing and comparing
481 the differential guiding effect imposed by the PAPL and the free area on cell migration. As shown in **Fig.**
482 **7b**, by tracking cell migration trajectories, we found that although the initial migration direction was
483 relatively uniform, it was significantly influenced by the PAPL and changed direction gradually,
484 preferentially migrating into the area where the PAPL remained. By calculating the angle θn
485 (counterclockwise) between the migration direction of each cell and the horizontal direction of the
486 viewport, and comparing it with the orientation angle of the interface between the PAPL and the free
487 area (θ_1 and θ_2 in **Fig. 7b**), we found that as the wound healing proceeded, the difference between θ_n and
488 θ_1 or θ_2 decreased (**Fig. 7c**). In the meantime, analysis of cell movement revealed an average speed of
489 18-43.2 μm/h during the collective cell migration and wound healing process (**Fig. 7d**). Above results
490 indicates that the cell migration direction gradually turned towards the PAPL, and away from the clear
491 area, in a manner approximately aligned with the interface between the PAPL and the free area. These
492 results suggest that the PAPL, although no longer possessing live-cell activity, still exhibits biological
493 activity and can interact with neighboring cells to regulate their movement. This is different from the
494 traditional free-boundary wound healing process and indicates a previously underexplored mechanism
495 that might play an important role in dictating collective cell migration and wound healing after HIFU-
496 induced ablation. Such mechanism poses an interesting question worthy of future studies.
497

498 **DISCUSSION**

499 In this study, we designed and built an enclosed cell culture device capable of simultaneously
500 achieving non-invasive ultrasound stimulation and long-term online live-cell imaging. Additionally, we
501 established an in vitro platform to explore the biological effects of ultrasound. In comparison to previous
502 experimental methods, this platform offers several advantages. Firstly, compared to conventional upright

503 FUS-imaging systems, the design of 45°-tilt angle of incidence built into the ECCD allows a clear and
504 uninterrupted acoustic path, thus it can achieve controllable FUS stimulation and ablation of cells within
505 a pre-defined target region, while cells outside the focal area could remain live, thus providing a
506 technical basis for investigating changes between cells subject to different levels of ultrasonic
507 stimulation in the same culture environment. Secondly, this platform is compatible with long-term cell
508 culture and real-time microscopic imaging, wherein multiple serial excitation and continuous imaging
509 experiments can be performed simultaneously. Thirdly, conventional upright imaging systems expose
510 the culture system to open environment and significantly increase the risk of contamination of the
511 culture. Even for short-term ultrasound stimulation, using upright imaging system could lead to
512 contamination observable within 24-48 hours. By avoiding the cell contamination risks associated with
513 previous methods, the ECCD platform allows the study of both the passive response of cells to short-
514 term FUS stimulation and the continuous observation of the active post-stimulation response of cells
515 over an extended period. Compared to conventional systems wherein FUS treatment and real-time
516 imaging are carried out using decoupled, open-environment devices, which often result in discontinuous
517 and unstable experimental conditions, the ECCD developed in this study provides an integrative
518 technical platform for on-demand spatiotemporal modulation of FUS treatment and continuous live-
519 imaging in a single, enclosed, stable environment, thereby facilitating the study of long-term biological
520 effects and responses after ultrasound therapy.

521 In previous studies, cavitation effect, which describes the process of bubble generation,
522 oscillation and collapse in target tissues under ultrasonic treatment, including stable cavitation and
523 inertial cavitation[38], is the most well-accepted effect of FUS. Stable cavitation is generally triggered by
524 low intensity ultrasound, which is characterized by alternating positive and negative pressures that cause
525 stable volume oscillations around the equilibrium position of the bubble. This effect can put cyclic stress

526 and shear forces on the cell, resulting in repairable, reversible perforation[30,39,40]. When the ultrasonic
527 intensity exceeds a certain threshold, inertial cavitation can cause violent volume oscillation and rapid
528 volume increase of bubbles, and finally lead to bubble rupture and collapse, producing high temperature
529 and high pressure, strong shock wave[41] or microjet[42], and reactive oxygen (ROS)[43], and lead to
530 reversible or irreversible perforation of cell membrane. Severe cases can lead to membrane tearing and
531 mechanical cell lysis[44, 45]. Nevertheless, direct experimental observation of cavitation bubbles' effect on
532 cell ablation are still limited except for a study by Wang *et al.* [33, 41, 44, 46]. In this study, such significant
533 cavitation occurs at the "initiation band of bubbles" at the periphery of the focal area in the ECCD,
534 which leads to rapid cell death and even the breakdown of the PAPL, thereby providing further
535 processive understanding of classical effects of FUS.

536 Despite various types of FUS-related effects reported in previous studies, they were studied separately
537 in different systems that vary in the spatial and temporal scales, as well as in the absence of a full view
538 of the integration of these effects throughout the focal region of FUS. By far, a single experimental
539 system to study and reconcile such diverse FUS-induced phenomena remains elusive. In this work, our
540 ECCD platform realizes real-time visual recording of the complete focal region of FUS, which serves as
541 an integrative system for studying the location-specific, mechanistically distinct effects throughout the
542 focal region. Indeed, we have observed a variety of biological effects in the focal region, including
543 acoustic streaming, cavitation effect, fine packet intense cracking and thermal effect, which includes and
544 extends beyond classical understanding of FUS effect. This platform not only establishes a convenient
545 system for the study of these effects, but also provides useful information for dissecting and future
546 rational optimization of FUS devices. Particularly, in addition to classical phenomena associated with
547 FUS, our results provide direct experimental evidence for the mechanolysis caused by HIFU, a
548 previously unreported biomechanical mechanism of ultrasound-induced cell ablation that occurs within

549 a specific area of cell ablation. In our study, we found that cavitation bubbles created under HIFU can
550 also cause mechanolysis of cells without collapse. In this case, because the bubble does not collapse
551 during the process of cell ablation, but has obvious volume growth, the mechanism of stable cavitation
552 and inertial cavitation proposed above is obviously different from that of previous studies. Therefore, the
553 mechanism of mechanolysis mediated by ultrasonic cavitation bubble formation and growth identified in
554 this study provides a previously unrecognized mechanism that may provide theoretical guidance for the
555 innovative development of future FUS applications.

556 It should be noted that the bubbles produced by the cavitation effect in this study are largely
557 derived from the dissolved gas in the culture system under high energy input from continuous FUS
558 waves. However, under the pulse wave with the same amplitude of 10% duty cycle, the transducer is
559 reduced to 1/10 of the power of the continuous wave (belonging to the intensity of LIFU), and cannot
560 input enough energy for the focal region, so the experimental results show that there is no significant
561 bubble formation under the pulse FUS. Nevertheless, our findings about the mechanolysis under HIFU
562 in this work can also extend to other contexts of applications wherein bubbles can be elicited through
563 assistive mechanisms under LIFU. At present, in the field of LIFU combined with microbubbles,
564 injection microbubbles are mostly used to provide cavitation nuclei[47], which has the advantage that the
565 addition of injection microbubbles can significantly reduce the cavitation threshold (about 100 times)[48],
566 and reduce the additional damage caused by high-intensity stimulation to tissues (LIFU intensity is 0.1-
567 1kW/cm^2 [49]). Therefore, by combining the mechanolysis principle found in this work with LIFU and
568 exogenous bubbles, it could inspire new strategies for future ultrasound-mediated cell ablation therapy.

569 The experimental platform developed in this study also provides a foundation for exploring long-
570 term biological responses following ultrasound stimulation, such as wound healing responses after
571 HIFU-induced ablation. Wound healing is a significant research topic in the field of medicine. For

572 studying the wound healing process, in vitro models, due to their more controllable environment
573 compared to in vivo models, are widely adopted for investigating wound healing mechanisms. Currently,
574 commonly used in vitro wound healing models are based on mechanical scratches or pre-occupied void
575 area[50, 51] to create free spaces for cells to migrate into. In addition to scratching, various methods such as
576 stamping, thermal stimulation, electric shocks, and laser illumination have been employed in monolayer
577 cell cultures to create "wounds"[52-55]. However, these models remain difficult to recapitulate the tissue
578 damage inflicted by ultrasound ablation, thereby hindering the understanding of the wound healing
579 process post-ultrasound treatment and limiting insights into the factors regulating the collective cell
580 migration during such wound healing. In this study, we achieved FUS ablation in a monolayer of cells in
581 vitro and observed a residual layer of cell remnants (the PAPL) left at the site of the ablation, providing
582 a unique model and method for understanding and studying the collective cell migration and wound
583 healing response after ultrasound treatment. Compared to traditional models of free-edge cell migration,
584 our model provides a more biomimetic representation of the ultrasound-inflicted wound. The
585 interactions between the PAPL and neighboring live cells further demonstrate its biological activity and
586 effects that can guide the direction of collective cell migration, a phenomenon not reported in previous
587 studies. Regarding such correlation between the PAPL and collective cell migration in wound healing,
588 we speculate that it might be related to intercellular connections between live cells and the PAPL.
589 Additionally, the release of lysophosphatidic acid during cell lysis and its activation of various
590 downstream signals might also contribute to this phenomenon[56, 57]. The specific mechanisms behind this
591 phenomenon await further exploration. In the future, this wound healing model might be used to explore
592 the therapeutic effects of FUS-based tumor ablation and the subsequent wound healing process in
593 adjacent normal tissues. Based on findings reported in this study, there might be more biomechanical

594 regulatory mechanisms and related application to be explored regarding the post-ablation wound healing
595 process.

596 In summary, the ECCD developed in this study integrates non-invasive ultrasound stimulation
597 and long-term live-cell imaging, providing a unique technological platform for in-depth exploration of
598 the mechanisms underlying ultrasound-induced biological effects. Based on this, we discovered
599 mechanism of ultrasound ablation via cavitation bubble formation and growth-mediated mechanolysis of
600 cells, adding another layer of our understanding of the biomechanical principles of ultrasound therapy.
601 The post-ablation wound healing model feature a PAPL layer and its interaction with collective cell
602 migration also offer new perspectives and methods for investigating tissue wound healing mechanisms.
603 The findings of this study might contribute to broaden our understanding of the biological effects of
604 ultrasound, and inspire advancements in the applications for FUS-based therapy.

605

606 **ACKNOWLEDGEMENTS**

607 We thank Dr. Haidong Wang for assistance in thermistor measurement. We thank Dr. Jiabin Zhang and
608 Dr. Feng Feng for assistance in ultrasound transducer calibration. We thank Dr. Yan Yi for the gift of
609 the ultrasound-absorbent rubber. We thank Dr. Jianbo Bai for the gift of the H2B-RFP MDCK cell line.
610 Y.S.'s work is supported by the National Natural Science Foundation of China (U21A20203, 12102229),
611 the National Key Research and Development Program of China (2021YFA0719301), the Oversea High-
612 level Scholar Introduction Program, Tsinghua University Dushi Program, and the Tsinghua University
613 Startup Funding.

614

615 **AUTHOR CONTRIBUTIONS**

616 Z.B. and Y.S. conceived the project; Z.B. designed and performed experiments; Z.B., Z.L., and Y.S.

617 analyzed data. Y.S. supervised the project. All authors contributed to the manuscript.

618

619 **COMPETING FINANCIAL INTERESTS**

620 The authors declare no competing financial interest.

621

622 **REFERENCES**

623 1. Krishna V, Sammartino F, Rezai A. A Review of the Current Therapies, Challenges, and Future
624 Directions of Transcranial Focused Ultrasound Technology: Advances in Diagnosis and
625 Treatment. *JAMA Neurol* **75**, 246-254 (2018).

626 2. Izadifar, Izadifar, Chapman, et al. An Introduction to High Intensity Focused Ultrasound:
627 Systematic Review on Principles, Devices, and Clinical Applications. *J. Clin. Med.* **9**, 460 (2020).

628 3. Meng, Y., Hynynen, et al. Applications of focused ultrasound in the brain: from thermoablation
629 to drug delivery. *Nat. Rev. Neurol.* **17**, 7-22 (2021).

630 4. Recker, F., Thudium, et al. Multidisciplinary management to optimize outcome of ultrasound-
631 guided high-intensity focused ultrasound (HIFU) in patients with uterine fibroids. *Sci. Rep.* **11**,
632 22768 (2021).

633 5. Yu Tang, Chun Chen, Binglei Jiang, et al. Bifidobacterium bifidum-Mediated Specific Delivery
634 of Nanoparticles for Tumor Therapy. *Int. J. Nanomed.* **16**, 4643-4659 (2021).

635 6. Lipsman, N., Meng, et al. Blood–brain barrier opening in Alzheimer's disease using MR-guided
636 focused ultrasound. *Nat. Commun.* **9**, 2336 (2018).

637 7. Shashank R. Sirsi, Mark A. Borden. State-of-the-art materials for ultrasound-triggered drug
638 delivery. *Adv. Drug Delivery Rev.* **72**, 3-14 (2014).

639 8. Kelsie F Timbie, Umara Afzal, Abhijit Date, et al. MR image-guided delivery of cisplatin-loaded
640 brain-penetrating nanoparticles to invasive glioma with focused ultrasound. *J. Controlled*
641 *Release* **263**, 120-131 (2017).

642 9. Saira Alli, Carlyn A. Figueiredo, Brian Golbourn, et al. Brainstem blood brain barrier disruption
643 using focused ultrasound: A demonstration of feasibility and enhanced doxorubicin delivery. *J.*
644 *Controlled Release* **281**, 29-41 (2018).

645 10. Cao Y, Chen Y, Yu T, et al. Drug Release from Phase-Changeable Nanodroplets Triggered by
646 Low-Intensity Focused Ultrasound. *Theranostics* **8**, 1327-1339 (2018).
647 11. Matos, Maria B. C. De, et al. Ultrasound-Sensitive Liposomes for Triggered Macromolecular
648 Drug Delivery: Formulation and In Vitro Characterization. *Frontiers in Pharmacology*, 10
649 (2019).
650 12. Ying Meng et al. MR-guided focused ultrasound enhances delivery of trastuzumab to Her2-
651 positive brain metastases. *Sci. Transl. Med.* **13**, 4011 (2021).
652 13. Stavarache, M. A., Petersen, N., et al. Safe and stable noninvasive focal gene delivery to the
653 mammalian brain following focused ultrasound. *J. Neurosurg.* **130**, 989-998 (2019).
654 14. Nickolai Sheikov, Nathan McDannold, Natalia Vykhodtseva, et al. Cellular mechanisms of the
655 blood-brain barrier opening induced by ultrasound in presence of microbubbles. *Ultrasound in*
656 *Medicine & Biology* **30**, 979-989 (2004).
657 15. Chen H, Konofagou EE. The Size of Blood–Brain Barrier Opening Induced by Focused
658 Ultrasound is Dictated by the Acoustic Pressure. *J. Cereb. Blood Flow Metab.* **34**, 1197-1204
659 (2014).
660 16. Colleen T. Curley et al. Augmentation of brain tumor interstitial flow via focused ultrasound
661 promotes brain-penetrating nanoparticle dispersion and transfection. *Sci. Adv.* **6**, 1344 (2020).
662 17. Miguel N. Centelles, Michael Wright, Po-Wah So, et al. Image-guided thermosensitive
663 liposomes for focused ultrasound drug delivery: Using NIRF-labelled lipids and topotecan to
664 visualise the effects of hyperthermia in tumours. *J. Controlled Release* **280**, 87-98 (2018).
665 18. Paul Cressey, Maral Amrahli, Po-Wah So, et al. Image-guided thermosensitive liposomes for
666 focused ultrasound enhanced co-delivery of carboplatin and SN-38 against triple negative breast
667 cancer in mice. *Biomaterials* **271**, 120758(2021).

668 19. Patricia C. Rinaldi, Joie P. Jones, Frederick Reines, et al. Modification by focused ultrasound
669 pulses of electrically evoked responses from an in vitro hippocampal preparation. *Brain Res.* **558**,
670 36-42 (1991).
671 20. Po-Hsiang Tsui, Shyh-Hau Wang, Chih-Chung Huang. In vitro effects of ultrasound with
672 different energies on the conduction properties of neural tissue. *Ultrasonics* **43**, 560-565 (2005).
673 21. David P. Darrow, Parker O'Brien, Thomas J. Richner, et al. Reversible neuroinhibition by
674 focused ultrasound is mediated by a thermal mechanism. *Brain Res.* **12**, 1439-1447 (2019).
675 22. T. Zhang et al. Transcranial Focused Ultrasound Stimulation of Periaqueductal Gray for
676 Analgesia. *IEEE Trans. Biomed. Eng.* **69**, 3155-3162 (2022).
677 23. Cotero, V., Graf, et al. Stimulation of the hepatoportal nerve plexus with focused ultrasound
678 restores glucose homoeostasis in diabetic mice, rats and swine. *Nat. Biomed. Eng.* **6**, 683–705
679 (2022).
680 24. Yixin Zhong, Yu Zhang, Jie Xu, et al. Low-Intensity Focused Ultrasound-Responsive Phase-
681 Transitional Nanoparticles for Thrombolysis without Vascular Damage: A Synergistic
682 Nonpharmaceutical Strategy. *ACS Nano* **13**, 3387-3403 (2019).
683 25. Zachs, D.P., Offutt, et al. Noninvasive ultrasound stimulation of the spleen to treat inflammatory
684 arthritis. *Nat. Commun.* **10**, 951 (2019).
685 26. Huerta, T.S., Devarajan, et al. Targeted peripheral focused ultrasound stimulation attenuates
686 obesity-induced metabolic and inflammatory dysfunctions. *Sci. Rep.* **11**, 5083 (2021).
687 27. Kennedy, J. High-intensity focused ultrasound in the treatment of solid tumours. *Nat. Rev.*
688 *Cancer* **5**, 321–327 (2005).
689 28. Kok H P, Cressman E N K, Ceelen W, et al. Heating technology for malignant tumors: A review.
690 *Int. J. Hyperthermia* **37**, 711-741 (2020).

691 29. Hynynen, K., et al. A scanned, focused, multiple transducer ultrasonic system for localized
692 hyperthermia treatments. *Int. J. Hyperthermia* **3**, 21-35 (1987).
693 30. Junru Wu, Wesley L. Nyborg. Ultrasound, cavitation bubbles and their interaction with cells.
694 *Adv. Drug Delivery Rev.* **60**, 1103-1116 (2008).
695 31. Hu, Zhang, Unger, et al. Focused Ultrasound-Induced Cavitation Sensitizes Cancer Cells to
696 Radiation Therapy and Hyperthermia. *Cells* **9**, 2595 (2020).
697 32. Manabu Kinoshita, Kullervo Hynynen. A novel method for the intracellular delivery of siRNA
698 using microbubble-enhanced focused ultrasound. *Biochem. Biophys. Res. Commun.* **335**, 393-
699 399 (2005).
700 33. Robyn K. Schlicher, Harish Radhakrishna, Timothy P. Tolentino, et al. Apkarian, Vladimir
701 Zarnitsyn, Mark R. Prausnitz, Mechanism of intracellular delivery by acoustic cavitation.
702 *Ultrasound in Medicine & Biology* **32**, 915-924 (2006).
703 34. Qiu, Zhihai, et al. The Mechanosensitive Ion Channel Piezo1 Significantly Mediates In Vitro
704 Ultrasonic Stimulation of Neurons. *iScience* **21**, (2019).
705 35. Yao-Shen Huang, Ching-Hsiang Fan, Ning Hsu, et al. Sonogenetic Modulation of Cellular
706 Activities Using an Engineered Auditory-Sensing Protein. *Nano Lett.* **20**, 1089-1100 (2020).
707 36. Hideki Kitamori, Iori Sumida, Tomomi Tsujimoto, et al. Evaluation of mouthpiece fixation
708 devices for head and neck radiotherapy patients fabricated in PolyJet photopolymer by a 3D
709 printer. *Physica Medica* **58**, 90-98 (2019).
710 37. Yuanru Zhao, Jingwen Xu, Yuanyuan Zhang, et al. Biomimetic redox-responsive prodrug
711 micelles with diselenide linkage for platinum nanozymes augmented sonodynamic/chemo
712 combined therapy of colon cancer. *Chem. Eng. J.* **472**, 144911 (2023).

713 38. Xuancheng Fu, Xiaoran Hu. Ultrasound-Controlled Prodrug Activation: Emerging Strategies in
714 Polymer Mechanochemistry and Sonodynamic Therapy. *ACS Appl. Bio Mater.*, 2024.
715 39. Hidemi Honda, Qing-Li Zhao, Takashi Kondo. Effects of dissolved gases and an echo contrast
716 agent on apoptosis induced by ultrasound and its mechanism via the mitochondria-caspase
717 pathway. *Ultrasound in Medicine & Biology* **28**, 673-682 (2002).
718 40. Alexander A. Doinikov, Ayache Bouakaz. Theoretical investigation of shear stress generated by
719 a contrast microbubble on the cell membrane as a mechanism for sonoporation. *J. Acoust. Soc.*
720 *Am.* **128**, 11–19 (2010).
721 41. Lokhandwalla, M., Sturtevant, et al. Mechanical haemolysis in shock wave lithotripsy (swl): i.
722 analysis of cell deformation due to swl flow-fields. *Phys. Med. Biol.* **46**, 413-413 (2001).
723 42. E.A Brujan. The role of cavitation microjets in the therapeutic applications of ultrasound.
724 *Ultrasound in Medicine & Biology* **30**, 381-387 (2004).
725 43. Zeyu Jiang, Wenjing Xiao, Qinrui Fu. Stimuli responsive nanosonosensitizers for sonodynamic
726 therapy. *J. Controlled Release* **361**, 547-567 (2023).
727 44. Boris Krasovitski, Victor Frenkel, Shy Shoham et al. Intramembrane cavitation as a unifying
728 mechanism for ultrasound-induced bioeffects. *Proc. Natl. Acad. Sci.* **108**, 3258-3263 (2011).
729 45. Liu Rengeng, Zhang Qianyu, Lang Yuehong et al. Sonodynamic therapy, a treatment developing
730 from photodynamic therapy. *Photodiagn. Photodyn. Ther.* **19**, 159-166 (2019).
731 46. Maochen Wang, Yi Zhang, Chenliang Cai et al. Acoustic and microbubble-cell parameters
732 Sonoporation-induced cell membrane permeabilization and cytoskeleton disassembly at varied.
733 *Sci. Rep.* **8**, 3885 (2018).
734 47. J. Deprez, G. Lajoinie, Y. Engelen et al. Opening doors with ultrasound and microbubbles:
735 Beating biological barriers to promote drug delivery. *Adv. Drug Delivery Rev.* **172**, 9-36 (2021).

736 48. Ambre Dauba, Anthony Delalande, Hermes A. S. Kamimura et al. Recent Advances on
737 Ultrasound Contrast Agents for Blood-Brain Barrier Opening with Focused Ultrasound.
738 *Pharmaceutics* **12**,1125 (2020).
739 49. Martijn Hoogenboom, Dylan Eikelenboom, Martijn H. den Brok et al. Mechanical High-
740 Intensity Focused Ultrasound Destruction of Soft Tissue: Working Mechanisms and Physiologic
741 Effects. *Ultrasound in Medicine & Biology* **41**, 1500-1517 (2015).
742 50. Tao, H., Berno, et al. In vitro human keratinocyte migration rates are associated with SNPs in the
743 KRT1 interval. *PLoS One* **2**, 697 (2007).
744 51. Nadine B. Wolf, Sarah Küchler, Michal R. Radowski, et al. Influences of opioids and
745 nanoparticles on in vitro wound healing models. *Eur. J. Pharm. Biopharm.* **73**, 34-42 (2009).
746 52. Stamm, Anne, Reimers, et al. In vitro wound healing assays – state of the art. *BioNanoMaterials*
747 **17**, 79-87 (2016).
748 53. Kai Safferling, Thomas Sütterlin, Kathi Westphal, et al. Wound healing revised: A novel
749 reepithelialization mechanism revealed by in vitro and in silico models. *J. Cell Biol.* **25**, 691–709
750 (2013).
751 54. Van Kilsdonk, Jeroen WJ, et al. An in vitro wound healing model for evaluation of dermal
752 substitutes. *Wound Repair and Regeneration* **21**, 890-896 (2013).
753 55. Ud‐Din, Sara, Ardeshir Bayat. Non‐animal models of wound healing in cutaneous repair: In
754 silico, in vitro, ex vivo, and in vivo models of wounds and scars in human skin. *Wound Repair*
755 *and Regeneration* **25**, 164-176 (2017).
756 56. George Broughton, I. I., Jeffrey E. Janis, et al. The basic science of wound healing. *Plast.*
757 *Reconstr. Surg.* **117**, 12S-34S (2006).

758 57. Schreml, Stephan, et al. Wound healing in the 21st century. *J. Am. Acad. Dermatol.* **63**, 866-881
759 (2010).
760
761
762
763

764 **FIGURES and FIGURE CAPTIONS**

765 **Figure 1**

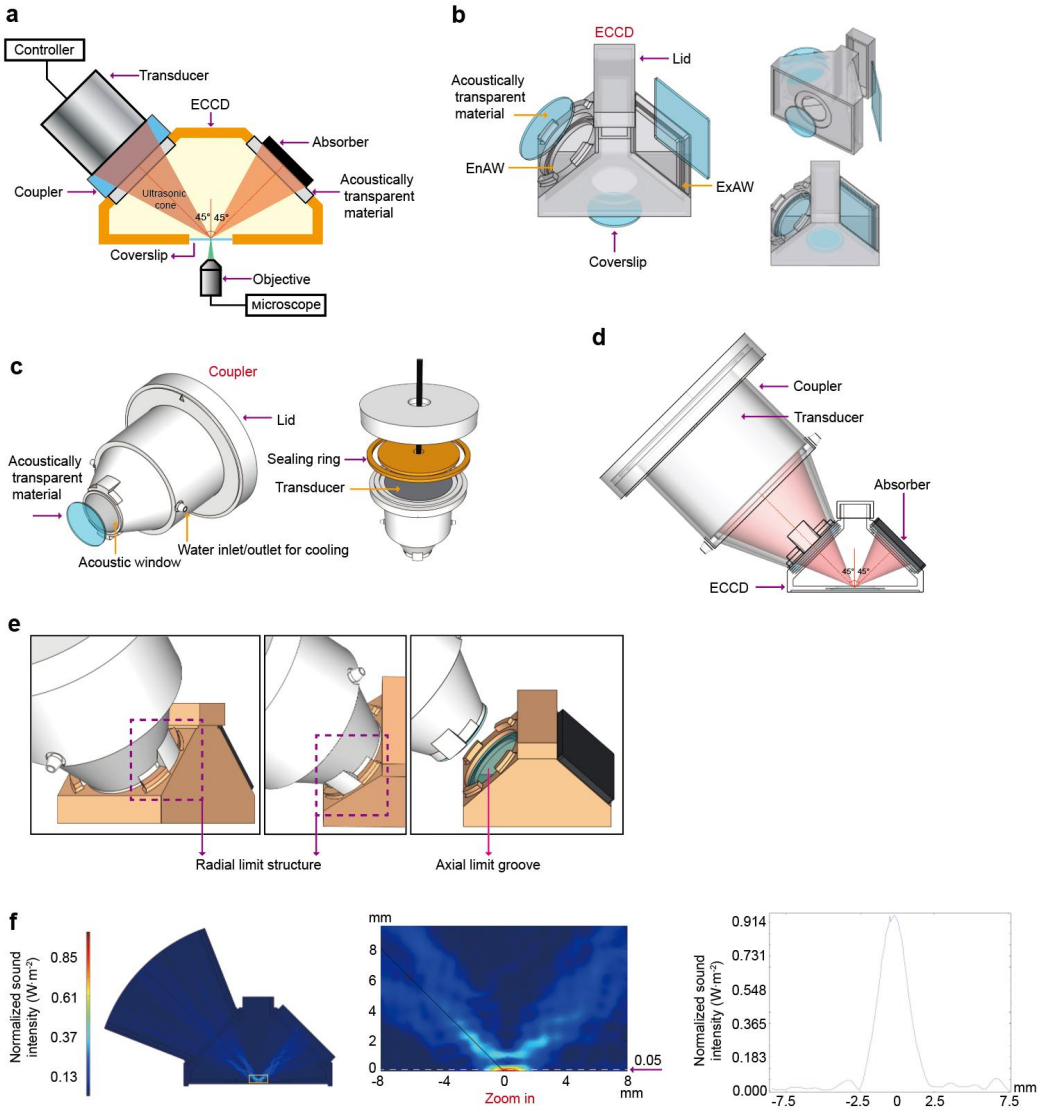

766

767 **Figure 1. Principle and design of the enclosed cell culture device compatible with focused**

768 **ultrasound stimulation and long-term microscopy imaging. (a)** Schematic diagram of the device

769 design and the acoustic pathway for focused ultrasound (FUS). **(b)** Structural design of the ECCD. **(c)**

770 Structural design of the FUS transducer coupler. **(d)** Schematic showing the assembly of the FUS

771 transducer and cell culture device with the acoustic pathway (schematic was drawn real component

772 proportions). **(e)** Design of the transducer coupler and positioning structure on the cell culture device. **(f)**

773 Computational results of the FUS acoustic field. Zoom-in displays the intensity field in the focal region.
774 The curve on the right shows the variation of intensity along the line drawn across the focal region, with
775 intensity represented by I_{sppa} (spatial peak pulsed average intensity, the maximum pulsed average
776 intensity on the acoustic field or a specified plane, in units of W/cm^2).
777

Figure 2

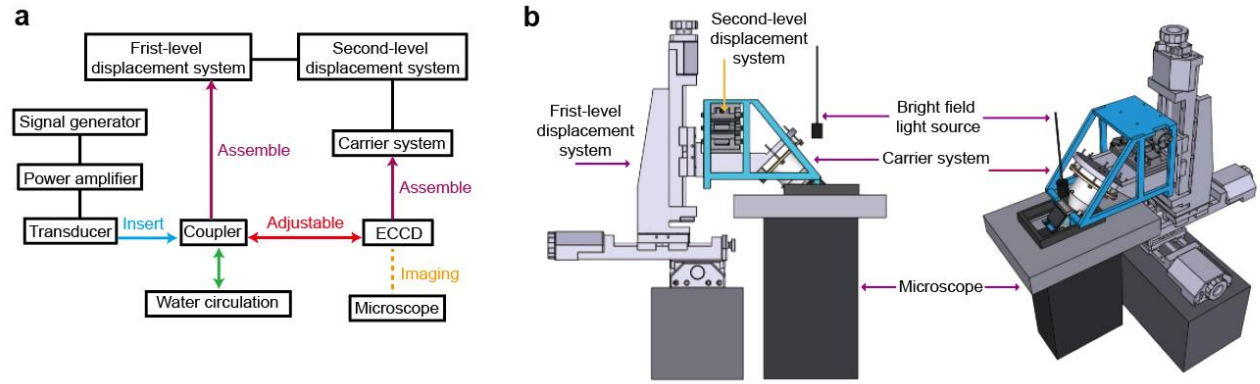

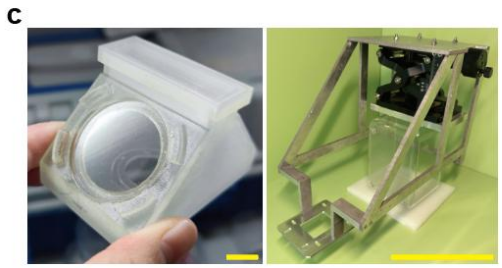

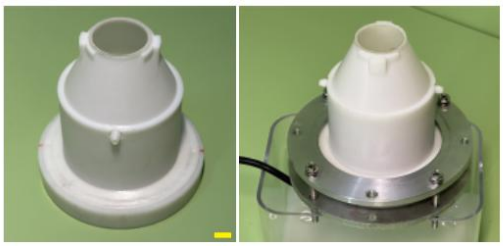

e

Materials	Sound velocity ($m \cdot s^{-1} \cdot 10^3$)	Density ($Kg \cdot m^{-3} \cdot 10^3$)	Acoustic impedance ($Kg \cdot m^{-2} \cdot s^{-1} \cdot 10^6$)
Plastic (T25 flask)	2.766	1.035	2.863
Plastic (35mm dish)	3.020	1.046	3.159
Silica gel	1.003	1.049	1.052
Acrylic plate	4.023	1.189	4.783
Plastic (culture plate)	2.753	1.044	2.874
MED610 light-cured resin	2.711	1.168	3.166
PDMS (4:1)	1.203	1.030	1.239
Pure water	1.500	1.000	1.500

f

Ratio of base to curing agent	Sound velocity ($m \cdot s^{-1} \cdot 10^3$)	Density ($Kg \cdot m^{-3} \cdot 10^3$)	Acoustic impedance ($Kg \cdot m^{-2} \cdot s^{-1} \cdot 10^6$)
10:1	1.058	1.034	1.094
5:1	1.123	1.031	1.157
4:1	1.203	1.030	1.239
3:1	1.115	1.029	1.148
2:1	1.059	1.025	1.085
1:1	1.052	1.024	1.077

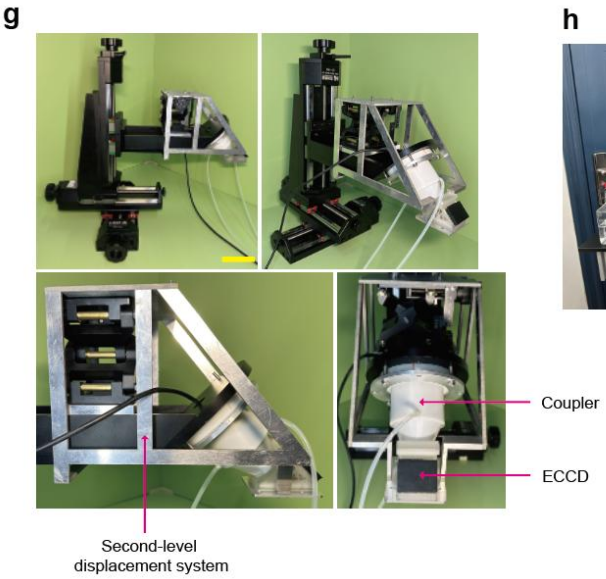

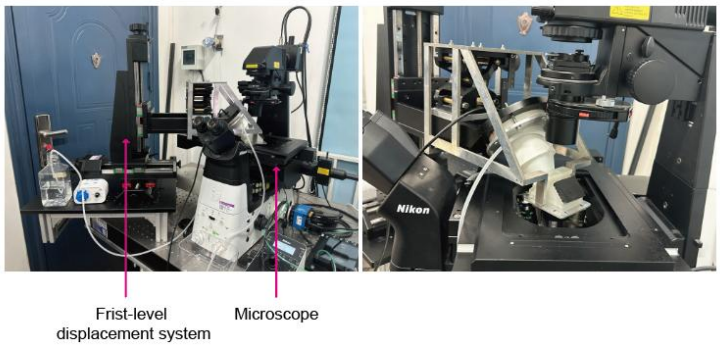

780 **Figure 2. Experimental setup for ultrasound stimulation and live-cell imaging based on the**
781 **ECCD.** **(a)** Flowchart showing the experimental setup and its operational procedure. **(b)** Design of the
782 primary and secondary displacement devices. **(c)** Photos of the ECCD and its tray system. The tray
783 system is connected to the displacement systems mentioned above. Scale bar: 10 mm. **(d)** Photos of the
784 FUS transducer coupler. Scale bar: 10 mm. **(e)** Selected acoustically transparent materials and their
785 measured acoustic parameters. Testing temperature: 25℃. **(f)** Table of acoustic parameters for PDMS
786 slab formed by mixing base liquid and curing agent in different proportions. Testing temperature: 25℃.
787 **(g)** Assembly of the displacement system, support system, ultrasound stimulation system, and cell
788 culture system. Scale bar: 10 cm. **(h)** Photos of the assembly of the ultrasound cell stimulation
789 experiment system and the microscope system.
790

Figure 3

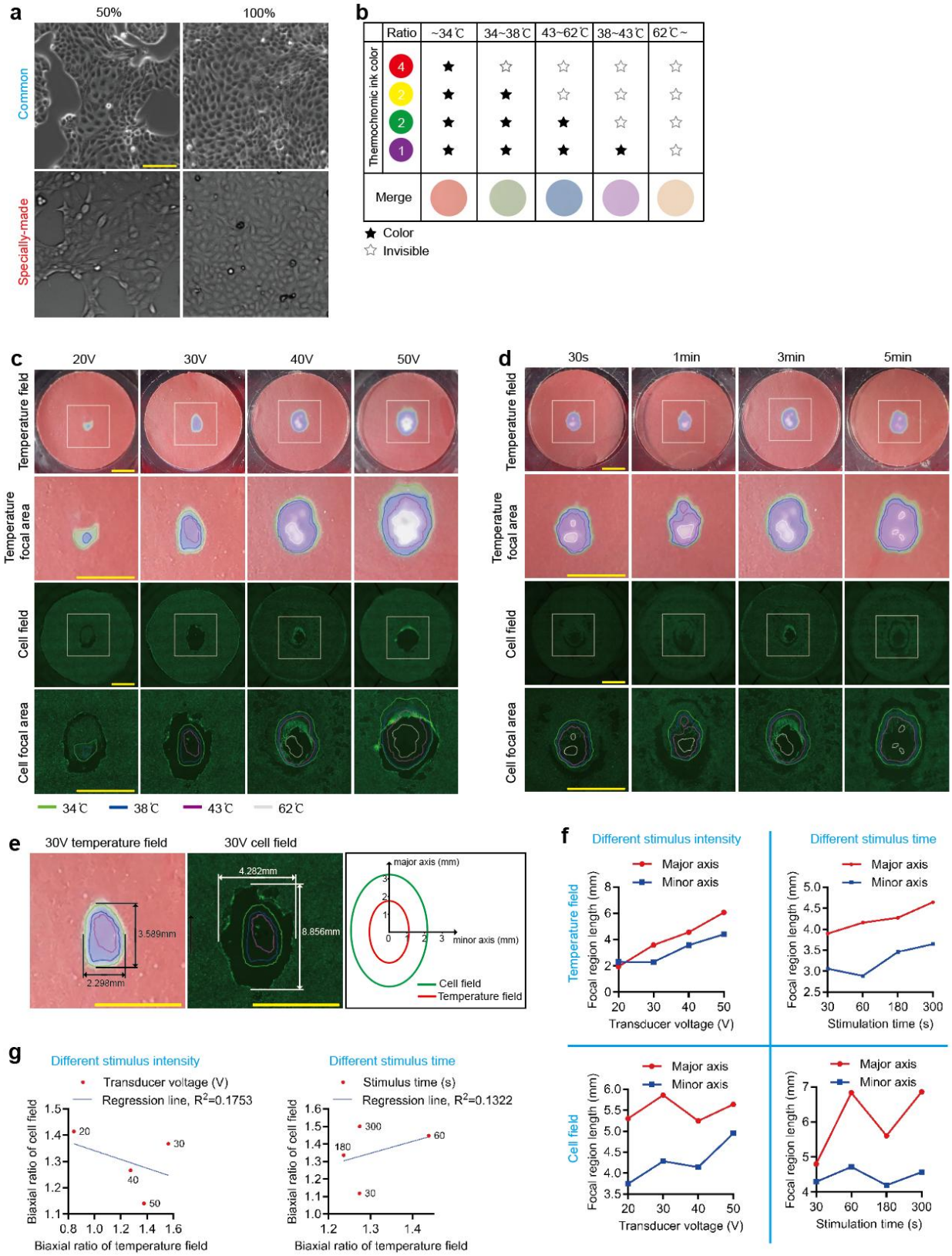
a
50%
100%
Common
Specially-made
b
Ratio
~34℃
34~38℃
43~62℃
38~43℃
62℃~
Thermochromic ink color
4
2
2
1
Merge
Color
Invisible
c
20V
30V
40V
50V
Temperature field
Temperature focal area
Cell field
Cell focal area
34℃
38℃
43℃
62℃
d
30s
1min
3min
5min
e
30V temperature field
30V cell field
3.589mm
2.298mm
4.282mm
8.856mm
major axis (mm)
minor axis (mm)
Cell field
Temperature field
f
Different stimulus intensity
Different stimulus time
Major axis
Minor axis
Temperature field
Cell field
Focal region length (mm)
Transducer voltage (V)
Stimulation time (s)
g
Different stimulus intensity
Different stimulus time
Transducer voltage (V)
Stimulus time (s)
Regression line, R2=0.1753
Regression line, R2=0.1322
Biaxial ratio of cell field
Biaxial ratio of temperature field

Figure 3. HIFU-induced cell ablation does not show significant correlation with ultrasound-caused thermal effect. (a) Bright-field images of MDCK cells cultured in regular 35 mm culture dishes and ECCD at confluence of 50% and 100%, respectively. Scale bar: 100 μm. **(b)** Table showing the temperature-dependent coloration of the four-color thermochromic ink at different temperatures. The mixing ratio is red: yellow: green: purple = 4:2:2:1. **(c)** The top row shows images of the thermosensitive color-changing sticker attached to the ECCD bottom changing color at the focal point under the influence of FUS. The FUS transducer emits continuous waves at a frequency of 1MHz with indicated voltages for 3 min. The second row shows zoom-in images of the focal region. The third row shows FITC fluorescence images at the focal point after the termination of FUS treatment. Live dye is used on cells, and non-fluorescent regions reflect cell ablation areas. The fourth row shows zoom-in images boxed in the third row. Scale bar: 5 mm. **(d)** The top row shows images of the thermosensitive color-changing sticker attached to the ECCD bottom changing color at the focal point under indicated duration of FUS treatment. The FUS transducer emits continuous waves at a voltage of 40 V. The second row shows zoom-in images of the focal region. The third row shows FITC fluorescence images at the focal point after the termination of FUS treatment. Live dye is used on cells, and non-fluorescent regions reflect cell ablation areas. The fourth row shows zoom-in images boxed in the third row. Scale bar: 5 mm. **(e)** The second image from the left shows the temperature field and cell field at the focal point under FUS exposure with a transducer voltage of 30 V and an exposure time of 3 min. The arrows indicate the size of the focal region along the major and minor axis. The third image is an ellipse fitted to the focal region. **(f)** Line charts showing the lengths of the major and minor axis of the focal region in the temperature field and cell field under different ultrasound intensities (representing different excitation voltages) and different exposure times. **(g)** Scatter plots of the aspect ratio of the focal region in the temperature field and cell field under different ultrasound intensities (*left*), with a line fitted through the least squares method (R^2=0.1753), and scatter plots of the aspect ratio of the focal region in

817 the temperature field and cell field under different FUS treatment duration (*right*), with a line fitted

818 through the least squares method (R^2=0.1322). The cells used in the above experiments were all wild-

819 type MDCK cell lines.

820
821

822 **Figure 4**

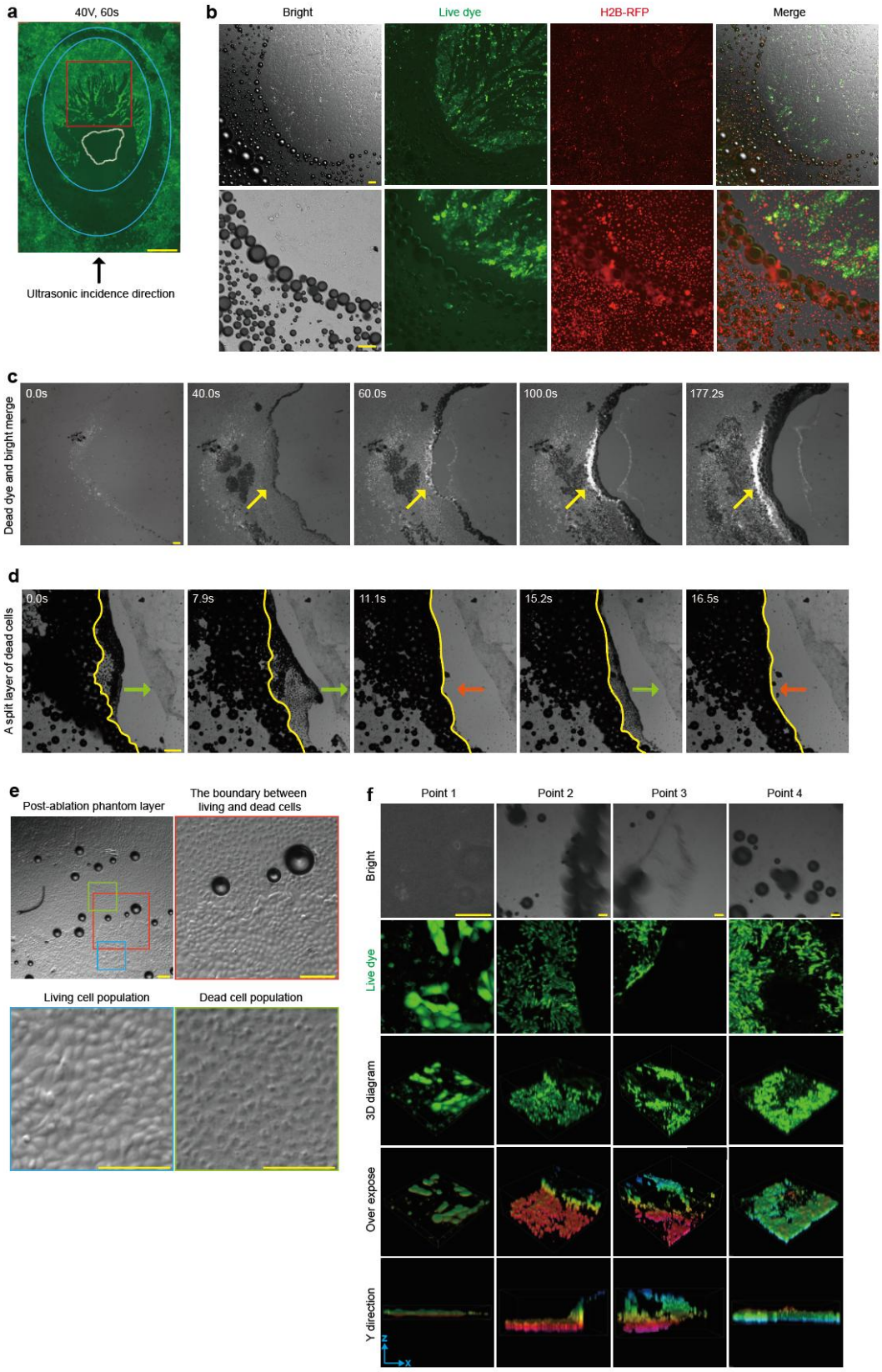

823

824 **Figure 4. Significant association between cell ablation zone and bubble generation zone under**
825 **FUS. (a)** FITC fluorescence images of cells taken after FUS treatment. The FUS transducer is powered
826 at 40 V, emits continuous waves at a frequency of 1 MHz, and has an exposure time of 1 min. The
827 direction of ultrasound incidence is indicated by black arrows. Live dye is used to label living cells, and
828 non-fluorescent regions reflect the cell ablation zone. Scale bar: 1 mm. The red box shows the streak-
829 like ablation domains in the focal area. The area surrounded by the two blue ovals is elliptical ablation
830 region where bubbles appear. The area enclosed by the white irregular lines is the area with a
831 temperature greater than 62 ℃ during FUS treatment. **(b)** Bright field, FITC and RFP fluorescence
832 images captured near the focal region after FUS treatment. The FUS transducer is powered at 40 V,
833 emits continuous waves at a frequency of 1 MHz, and has an exposure time of 3 min. Bubbles are
834 opaque and spherical under bright field. H2B-RFP MDCK cells are used. Live dye is used on cells, and
835 non-fluorescent regions reflect the cell ablation zone. Scale bar: 100 μm. **(c)** Time-lapse micrographs
836 captured under bright field and RFP fluorescence during FUS treatment. Yellow arrows indicate bands
837 of bubbles. The FUS transducer is powered at 40 V, emits continuous waves at a frequency of 1 MHz.
838 Cells are stained with red fluorescent dead cell dye, and fluorescent regions reflect the cell ablation zone.
839 Scale bar: 100 μm. (The time-stamp starts from the first image shown here) **(d)** Images captured at the
840 edge of the focal region under bright field during FUS exposure. Yellow lines represent the edges of
841 stable bubble bands. Red and green arrows indicate the expansion and retreat directions of the
842 movement of bubble clusters. The FUS transducer is powered at 40 V, emits continuous waves at a
843 frequency of 1 MHz. Scale bar: 100 μm. (The time-stamp starts from the first image shown here) **(e)** The
844 top-left image shows the bright field microscopic image after ultrasound exposure. The FUS transducer
845 is powered at 40 V, emits continuous waves at a frequency of 1 MHz, and has an exposure time of 3 min.
846 The other three images are zoom-in views of the areas boxed in by different color squares in the top-left

847 image. The bubble zone is spatially correlated with the cell ablation zone, and the morphology of the
848 post-ablation phantom layer (PAPL) after cell ablation is significantly different from the live cell
849 monolayer. Scale bar: 100 μm. **(f)** The top two rows show bright field and FITC fluorescence images
850 after FUS exposure. The FUS transducer is powered at 40 V, emits continuous waves at a frequency of 1
851 MHz, and has an exposure time of 3 min. Live dye is used on cells, and non-fluorescent regions reflect
852 the cell ablation zone. The bottom three rows show 3D reconstructed microscopic images of the PAPL
853 and its adjacent live cell monolayer. Point 1 shows the PAPL that remained in its original place; Points
854 2-3 show PAPL rupture and peeled off the substrate by bubbles, along with some live cell monolayer
855 connected to it; Point 4 shows the PAPL forming a "dome" shape, with its central part detached but
856 peripheral part connect to the live cell monolayer on the substrate. Scale bar: 100 μm. The cells used in
857 **Fig. 4a&c-f** were wild-type MDCK cells.
858

859 **Figure 5**

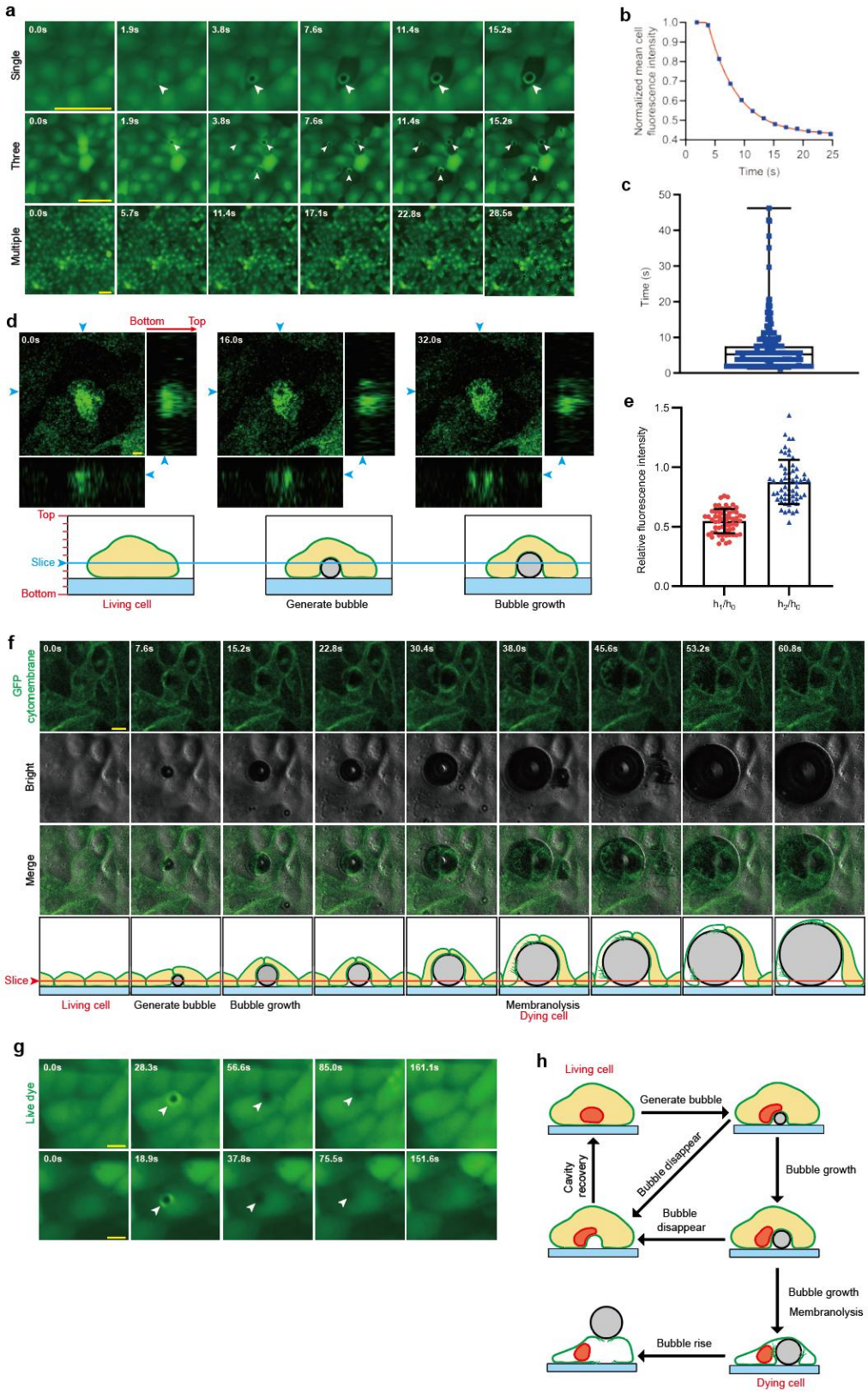

860

861 **Figure 5. Subcellular bubble formation and FUS-induced mechanolysis of the cell. (a)** Time-
862 lapse FITC fluorescence micrographs of MDCK cells under FUS treatment. The three rows represent
863 images where bubbles appear in a single cell, three different cells, and multiple cells, respectively. Live
864 dye is used on cells, and the disappearance of the fluorescent signal reflects cell ablation. The FUS
865 transducer is powered at 40 V, emits continuous waves at a frequency of 1 MHz. Scale bar: 50 μm. **(b)**
866 Scatter plot and interpolated curve showing the average fluorescence intensity of the cell cytoplasm
867 (excluding bubble area) over time for the cells shown in the first row of images in **(a)**. **(c)** Scatter plot of
868 the time taken from bubble appearance to the average fluorescence intensity of the cell dropping to the
869 background fluorescence intensity. (box: 25% - 75%, bar-in-box: median, and whiskers: min and max).
870 n = 3 independent experiments; n_{cell} = 350. The FUS transducer is powered at 40 V, emits continuous
871 waves at a frequency of 1 MHz. **(d)** FITC fluorescence images showing bubbles generated at cells
872 during FUS exposure. The X-Y, X-Z, and Y-Z images were shown for the cell. The green area on the
873 image represents the cell region, and the black area appearing in the cell region represents the bubble
874 region. The intersection points correspond to the center points of the bubbles. Cells are MDCK cells
875 expressing GFP on the cell membrane. The FUS transducer is powered at 40 V, emits continuous waves
876 at a frequency of 1 MHz. Scale bar: 10 μm. **(e)** Analysis of fluorescence intensity at the location of the
877 bubble. The fluorescence intensity at the center of the bubble causing cell ablation is denoted as h_1 when
878 it first appears and h_2 after it caused cell ablation, and the fluorescence intensity at that position before
879 bubble generation is denoted as h_0. The scatter plot shows h_1/h_0 and h_2/h_0. Data were plotted as mean ±
880 s.d. n = 3 independent experiments; $n_{samples}$ = 59. **(f)** Bright field and FITC fluorescence micrographs
881 showing bubbles generated underneath the cell and eventually causing cell membrane rupture during
882 FUS exposure. GFP-cytomembrane MDCK cells were used. Scale bar: 10 μm. **(g)** Time-lapse FITC
883 fluorescence micrographs showing bubbles appearing and disappearing underneath the cell during FUS

884 treatment. Live dye is added to the cells. The FUS transducer is powered at 40 V, emits continuous
885 waves at a frequency of 1 MHz. Scale bar: 10 μm. **(h)** Schematic of different types of interactions
886 between HIFU-induced bubbles and cells observed in this study. The cells used in above experiments
887 were wild-type MDCK cells.
888

889 **Figure 6**

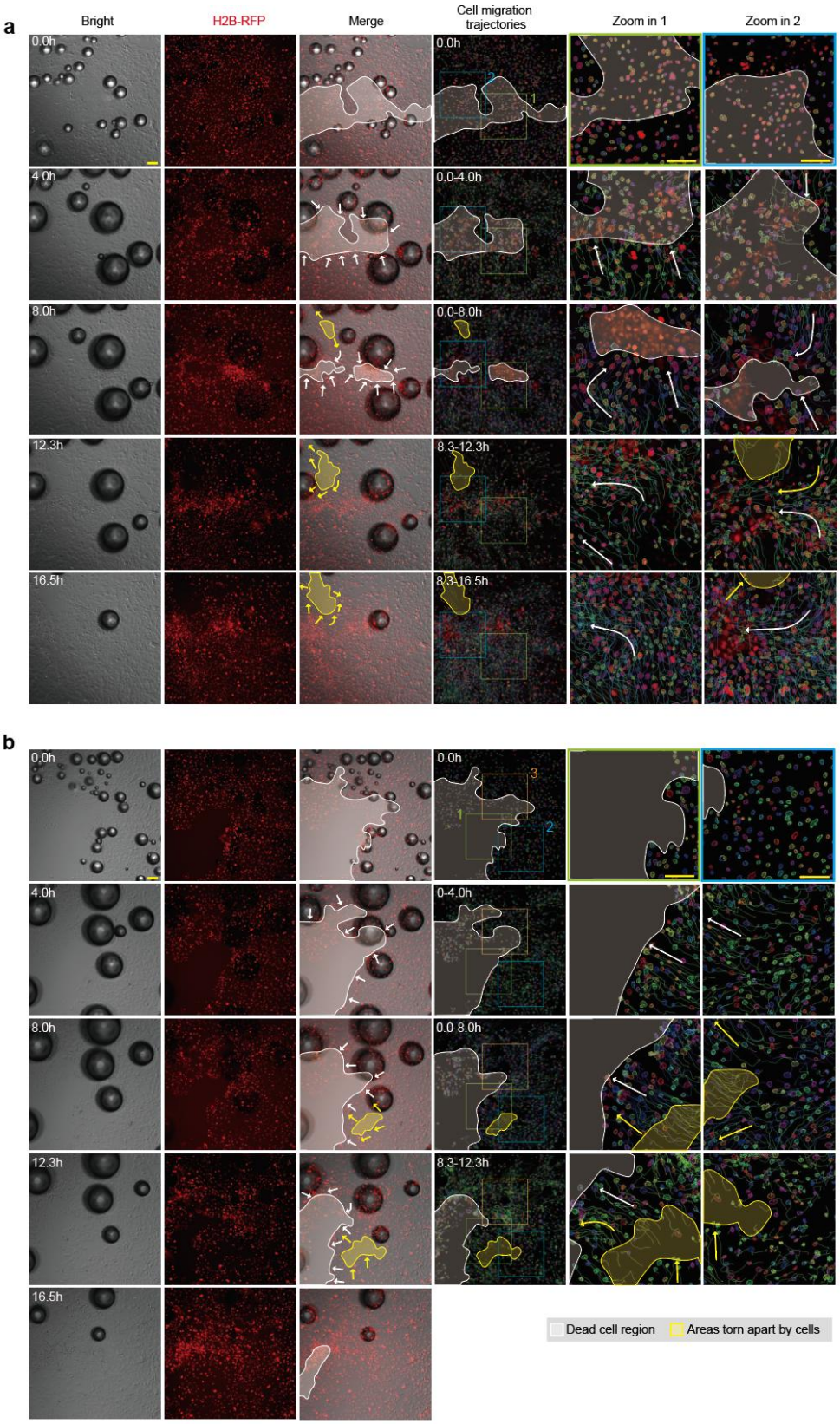

890

891 **Figure 6. Observation of collective cell migration and wound healing after FUS ablation. (a, b)**
892 The first three columns depict time-lapse bright-field and RFP fluorescence micrographs showing the
893 collective migration of live cells towards the PAPL or clear area after HIFU-induced ablation. In the
894 third column, the white area represents the PAPL (with remaining RFP-labeled cell nuclei but no
895 movement) or the clear area (where PAPL detached), with white arrows indicating the direction of
896 collective cell migration. The yellow area represents secondary tissue gaps that appear during the
897 primary wound healing process, largely due to the different directions and speeds of cell migration
898 within the live cell monolayer, with yellow arrows indicating the cell migration direction. The fourth
899 column shows the trajectories of individual cell nuclei during the collective migration (Colored line).
900 The fifth to sixth columns in **(a)** and the fifth to seventh columns in **(b)** provide zoom-in views of the
901 boxed regions in the fourth column. Scale bar: 100 μm. White arrows indicate the location of bubbles.
902 The cells used in above experiments were H2B-RFP MDCK cells
903

904 **Figure 7**

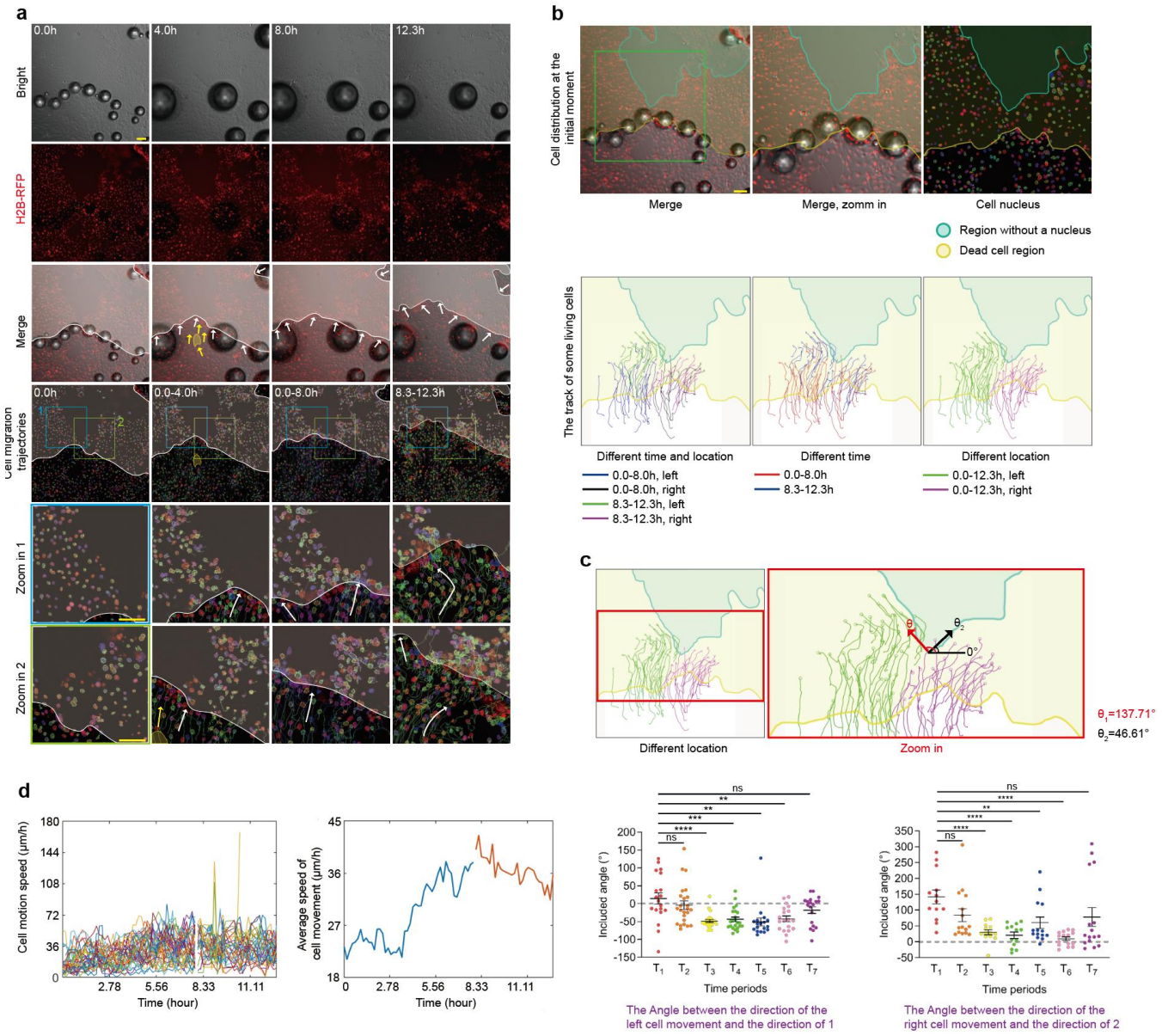

905
906
907 **Figure 7. Effect of the PAPL on the collective migration and wound healing after HIFU-induced**

908 **ablation. (a)** The first three rows show time-lapse bright-field and RFP fluorescence micrographs after

909 focused exposure, illustrating the collective migration of live cells toward the PAPL or the free area

910 (where the PAPL has detached). In the third row, the white area represents the PAPL or the free area,

911 with white arrows indicating cell migration direction. The yellow area represents secondary gaps formed

912 in the collectively migration cell sheet nearby the wound, largely due to different directions and speeds

913 of cells within the monolayer. Yellow arrows indicate the cell migration direction at the edge of the free
914 area. The fourth row displays the trajectories of individual cell nuclei during the wound healing process.
915 The fifth to sixth rows provide zoom-in views of the boxed regions in the fourth row. Scale bar: 100 μm.
916 **(b)** Trajectories of individual cells during collective cell migration. Scale bar: 100 μm. **(c)** Angles
917 between the migration direction of individual cells and the orientation of the interface between the
918 PAPL and the free area at different time points as indicated. (T_1: 0.00-0.67 h; T_2: 2.33-3.00 h; T_3: 4.67-
919 5.33 h; T_4: 7.00-7.67 h; T_5: 8.50-9.17; T_6: 10.17-10.83h; T_7: 11.83-12.50 h). Data were plotted as mean
920 ± s.e.m. * $P < 0.05$, ** $P < 0.01$, *** $P < 0.001$, **** $P < 0.0001$. **(d)** Line graphs depicting the
921 migration speed of individual cells (left) and the average speed of the cell population (right) during
922 collective migration.
923
924
925
926
927
928